Colloid dynamics in semiflexible polymer solutions

Ji Yeon Huh and Eric M. Furst*
Department of Chemical Engineering, Colburn Laboratory, University of Delaware, 150 Academy Street, Newark, Delaware 19716, USA
(Received 2 March 2006; published 12 September 2006)

We investigate the dynamics of monodisperse colloidal polystyrene particles suspended in solutions of the semiflexible polymer filamentous actin, over a range of filament lengths that either exceed or are substantially less than the particle radius. The filament length is controlled by the capping protein gelsolin, and particle surface chemistries that minimize the adsorption of filaments are used. The particle dynamics are measured on short time scales using diffusing wave spectroscopy. A sharp transition in the initial particle diffusivity marks the expected shift from a dilute to a tightly entangled polymer network as the filament average length increases. In both the dilute and entangled regimes, the measured particle dynamics are compared with the theories of rodlike and semiflexible polymer solution rheology using the generalized Stokes-Einstein relationship. In the dilute limit, the particle dynamics are in good agreement with theory. However, in the tightly entangled regime, the particle response is consistent with polymer depleted near the surfaces of the particles. The magnitude of the depletion layer thickness depends strongly on particle size and weakly on filament length. This behavior is in agreement with nonlocal entropic repulsions and the loss of conformational entropy associated with rodlike molecules near impenetrable particles. These results illustrate the use of microrheology as a method to investigate local structure and dynamics in colloid-polymer solutions.

DOI: 10.1103/PhysRevE.74.031802 PACS number(s): 83.80.Rs, 82.70.Dd, 05.40.Jc, 83.60.Bc

I. INTRODUCTION

The multicomponent interactions and structure in colloid-polymer solutions underlie the phase behavior, viscoelasticity, stability, and vitrification of these systems [1,2]. In turn, the unique properties of colloid-polymer solutions and other filled systems play significant roles in many industrial applications. Suspensions of particles in polymer solutions occur in a remarkable range of technologies and products, from paints and coatings to consumer and personal care products [3].

The behavior of colloid-polymer solutions depends on the nature of the colloid-colloid, colloid-polymer, and polymer-polymer interaction and correlations [4]. For instance, it has long been recognized that dilute solutions of nonadsorbing polymer induce attractive depletion interactions between colloidal particles [5]. Theory treats the polymer as an ideal solution of hard spheres with radius equal to the polymer's radius of gyration R_g. Even these fairly simple systems exhibit rich phase behavior, including regions of coexistence between fluid-fluid and fluid-crystal phases [6–8]. However, as the polymer concentration exceeds the entanglement transition, the polymer size becomes greater than that of the dispersed particles, or the particle concentration becomes high, the structural correlations, amenable to treatment by mean-field descriptions in the simplest cases, become more complex. Theoretical approaches using refined models of the polymer-particle direct correlations illustrate the complex nature of the colloid-polymer and polymer-polymer interactions. For instance, the modified polymer reduced interaction site model based on the Percus-Yevick closure approximation (PRISM-mPY) takes into account local entropic repulsions between the particle and polymers and the loss of conformational entropy of polymer segments close to the particles [9].

Studies of polymer-colloid interactions and structure are critical for emerging applications, including nanocomposites and protein crystallization [10,11]. Filled semiflexible polymer networks are of particular interest, because semiflexibility leads to additional complexity due to polymer alignment at interfaces and the existence of an isotropic-nematic transition at high polymer concentrations [12]. Semiflexible polymers exist in an intermediate regime of polymer contour length L and persistence length L_p, where $L_p/L \sim 1$, in contrast to flexible ($L_p/L \ll 1$) and rodlike ($L_p/L \gg 1$) polymers. Examples include poly(benzyl glutamate) (PBLG), cellulose, xanthan, Kevlar, wormlike micellar solutions, tobacco mosaic virus, filamentous actin (F-actin), and DNA [12–14]. In industrial applications, semiflexible polymers are attractive rheological modifiers, since significant viscoelastic properties can be introduced using a relatively small amount of material [15]. The fluid structure correlations of filled semiflexible networks are dependent on the relative ratios of the particle radius a, polymer contour length L, persistence length L_p, polymer concentration c, and particle volume fraction ϕ. Figure 1 illustrates the effects these parameters are expected to have on the local polymer network structure. In the limit of $L/L_p \ll 1$ and $a/L \gg 1$, unentangled rods surround dilute particles. Such conditions have been shown to induce a depletion attraction between particles, analogous to nonadsorbing flexible polymers [16–18]. Increasing the polymer length while maintaining the same total polymer contour length density, the filaments form loosely entangled (LE) and tightly entangled (TE) networks around the particles [19]. The fluid structure in these regimes has been largely unstudied. From this point, increasing the colloid volume fraction will again change the local structure; emerging theoretical

*Corresponding author. Electronic address: furst@che.udel.edu

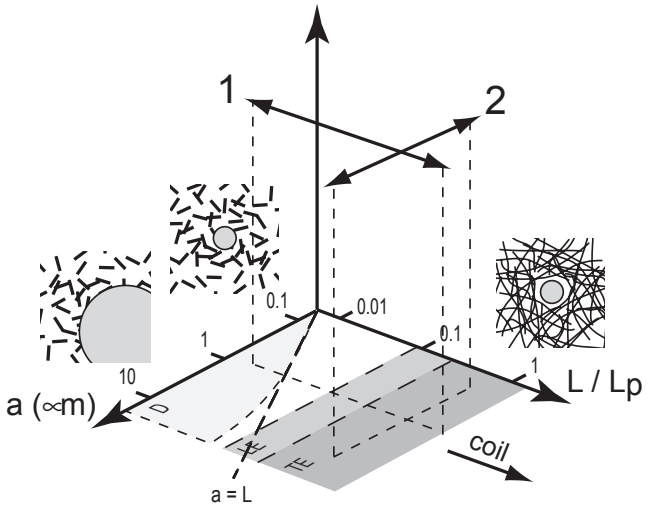

FIG. 1. The multicomponent correlations of filled semiflexible networks are dependent on the relative ratios of the particle radius a, polymer contour length L, persistence length L_p, polymer concentration c, and particle volume fraction ϕ. D, LE, and TE indicate dilute, loosely entangled, and tightly entangled regimes, respectively. In this work, we investigate the response of particles as the filament length is changed, illustrated by the line labeled 1. The effect of particle size was investigated previously (line labeled 2) [30].

frameworks suggest that colloid correlations are "imprinted" on the surrounding network [4].

In this paper, we report investigations of the structure and response of colloid-semiflexible polymer solutions of filamentous actin (F-actin) using light scattering measurements of the suspended particle dynamics. Numerous experimental and theoretical studies have focused on the rheology and microrheology of F-actin, a helical protein filament with persistence length $L_p \approx 17$ μm and an average steric diameter 7nm [20,21]. F-actin plays a critical role in the mechanical response and other cellular functions of eukaryotic cells [22,23]. F-actin has also been used extensively as a model system to study semiflexible polymer dynamics, structure, and rheology [24–28]. It is amenable to fluorescent labeling and can be extracted and purified in relatively large amounts from muscle tissue [29].

Previously it was demonstrated that the dynamics of colloidal particles in tightly entangled networks of F-actin are consistent with the formation of a polymer-depleted region surrounding the particles when measures are taken to *minimize* filament adhesion to the particles [30]. The magnitude of this depleted layer, and its dependence on particle size, are consistent with a mechanism in which filaments are excluded from a corona surrounding each particle due to its long length and rigidity [19]. To investigate this local structure further, in this work, we focus on the effect of the contour length of the filaments on the depletion layer.

The remainder of the paper is organized as follows. We first detail our experimental methods. Next, we present the dynamics of particles in solutions of F-actin, and discuss the behavior of the particle dynamics as the filament length is increased at constant polymer concentration. From these results, we identify the dilute and entangled regimes of the polymer. Using the generalized Stokes-Einstein equation, we compare the particle dynamics to the dynamics expected from theories of dilute and entangled rodlike and semiflexible polymers. We conclude with final remarks and future directions for this work.

II. EXPERIMENT

Frozen monomeric actin (G-actin, MW=42 kDa) purified from rabbit skeletal muscle (Lot #056, Cytoskeleton, Denver, CO) is dissolved in G-buffer [5 mM Tris-HCl pH 8.0, 0.2 mM ATP, 0.2 mM $CaCl_2$, 0.5 mM dithiothreitol (DTT) and 0.005% NaN_3] at 4 °C for 24 h. G-actin is mixed with monodisperse colloidal particles (described below), and polymerized into F-actin by increasing the KCl concentration to 50 mM and $MgCl_2$ to 1 mM using a 10X solution in G-buffer. The final particle volume fraction is ϕ=0.01, and the final actin concentration is 0.63 mg/ml, corresponding to the network mesh size $\xi \sim 0.378$ μm for unshortened filaments [31]. Gelsolin from human plasma (MW=83 kDa, Cytoskeleton) is used to adjust the mean filament length, L, by adding to G-actin before initiating polymerization. According to Janmey *et al.* [32], L is calculated via the relation $L = 1/370 r_{G:A}$ μm, where $r_{G:A}$ denotes the molar ratio of gelsolin to actin. The mean filament length of F-actin polymerized in the presence of gelsolin spans the range from L=0.053 −20 μm, assuming that the average filament length in the absence of gelsolin is approximately 20 μm [26].

The particles used in this study are monodisperse polystyrene (PS) microspheres ($2a$=1.07 μm and 3.21 μm diameter, Polysciences, Inc.), with adsorbed bovine serum albumin (BSA, Sigma-Aldrich) to reduce actin binding to the particle surface [30,33]. They are prepared by first washing the particles with successive centrifugation and redispersion steps using purified water, then incubating overnight in a 200 mg/ml BSA solution. The particles are again washed three to five times by successive centrifugation and redispersion steps to remove unbound BSA or impurities. As an alternative surface treatment, we compare the BSA-adsorbed PS particles to microspheres with a dense monolayer of covalently attached poly(ethylene glycol) (PEG). To prepare PEG-coated particles (PS-PEG), we react N-hydroxysuccinimide (NHS, Sigma-Aldrich) active esters (mPEG-SPA (mPEG-succinimidyl propionate), NEKTAR, MW=5000 Da) to amine modified PS spheres (0.91±0.022 μm, Spherotech.). Amine modified PS particles of 0.5–5 mg/ml are mixed with onefold to tenfold excess of mPEG-SPA in borate buffer at pH 8.5 for 90 min. Then, the particles are washed with pure borate buffer, recovered, and stored at 4 °C. Both BSA- and PEG-coated particles are observed under a microscope to verify that they are stable and do not aggregate.

Diffusing wave spectroscopy (DWS) experiments are performed in a transmission geometry with a plane-wave excitation using an etalon-equipped Ar^+ laser (wavelength 514.5 nm) [34]. Light is collected by a collimated single-mode fiber optic, which is split to two photomultiplier tubes (PMT), each with a dedicated amplifier and discriminator.

The intensity autocorrelation of the scattered light $\langle I(0)I(t)\rangle/\langle I\rangle^2$ is calculated using a pseudo-cross-correlation mode over delay times 25 ns to 1 s using a correlator (Brookhaven Instruments, BI-9000). The field auto correlation function $g^{(1)}(t)$ is obtained via the Siegert relation $\langle I(0)I(t)\rangle/\langle I\rangle^2 = 1+\beta|g_1(t)^2|$ where the intercept β accounts for the optical properties of our apparatus. We numerically calculate the mean-squared displacement (MSD) from the field autocorrelation function for the transmission geometry by the equation [34]

$$g^{(1)}(t) = \frac{\left(\frac{l}{l^*}+\frac{4}{3}\right)\sqrt{k_0^2\langle\Delta r^2(t)\rangle}}{1+\frac{4}{9}k_0^2\langle\Delta r^2(t)\rangle\sinh\left[\left(\frac{l}{l*}\right)\sqrt{k_0^2\langle\Delta r^2(t)\rangle}\right]+\frac{4}{3}\sqrt{k_0^2\langle\Delta r^2(t)\rangle\cosh\left(\frac{l}{l*}\right)\sqrt{k_0^2\langle\Delta r^2(t)\rangle}}}, \tag{1}$$

where $l=4$ mm is the scattering cell thickness. The photon mean free path l^*, over which the direction of the scattered light is completely randomized, is measured by comparing the average transmitted light intensity against a standard sample with a known value of l^*. Typical l^* values are 0.2 and 0.6 mm for 1 and 3 μm diameter particles, respectively. Further details of the experiment and analysis are found in Ref. [30].

III. RESULTS AND DISCUSSION

A. Mean-squared displacement

The mean-squared displacement $\langle\Delta r^2(t)\rangle$ of colloidal particles dispersed in 0.63 mg/ml F-actin solutions for a range of filament lengths are shown in Fig. 2. In all cases, the mean-squared displacement exhibits a power-law behavior, $\langle\Delta r^2(t)\rangle\sim t^\alpha$. The scaling exponent α reflects diffusive or slightly subdiffusive dynamics, and decreases as the filament length increases. The values of α, which range between 0.95 and 1.0, are summarized in Table I. From the initial slope of $\langle\Delta r^2(t)\rangle$, we calculate the short-time self-diffusion coefficient of the particles, D_0, for each filament length. Similar to the scaling behavior, Fig. 3 shows that D_0 decreases with increasing filament length. Notably, however, there is an inflection in the data near the average filament length $L=1$ μm. For average filament lengths above $L=1$ μm, the decrease in D_0 is a stronger function of increasing filament length.

The filament length at the inflection point in D_0 shown in Fig. 3 marks the transition from the dilute to the entangled regime of F-actin. As decreasing amounts of gelsolin are added, the filaments become longer, and they form entangled solutions. Recently, Hinner *et al.* [35] determined that the entanglement transition in F-actin occurs at the concentration (in units of mg/mL),

$$c^* = \frac{7\times 2^{1/4}L_p^{1/2}\xi_1^2}{3\pi(5L/7)^{5/2}}. \tag{2}$$

The parameter $\xi_1=0.35$ is the apparent mesh size of an F-actin solution at the concentration 1 mg/ml determined from fluorescence recovery after photobleaching experiments [13]. The entanglement concentration is a factor of $c^*/\bar{c}\approx 2.0(L_p/L)^{1/2}$ larger than the initial overlap concentration, $\bar{c}$.

In Fig. 4, calculated values of the overlap concentration $\bar{c}$ and entanglement concentration c^* are shown for each of the average filament lengths investigated. At $L=1.2$ μm, c^* is identical to the experimental actin concentration 0.63 mg/mL. This value is in excellent agreement with the point of inflection in Fig. 3. Therefore, the trend of D_0 as the filament length is changed at a fixed actin monomer concentration provides an accurate indicator of the transition between the dilute and tightly entangled regimes. Not surprisingly, the initial particle diffusion coefficient is insensitive to the overlap concentration. With $\bar{c}=0.63$ mg/mL, the calculated filament length marking the boundary between weak overlap and the dilute regime is $L=0.5$ μm. In the overlap regime, the rotation of the polymer is hindered, but the bending mode fluctuations of the polymers, which dominate at the time scales probed here, are unaffected [12,19].

Using the generalized Stokes-Einstein relationship (GSER), the dynamics of colloids dispersed in F-actin solutions can be compared to theories that describe the rheology of dilute and entangled semiflexible polymers. We calculate the frequency-dependent modulus amplitude from the particle mean-squared displacements measured using light scattering by [36]

$$|G^*(\omega)| = \frac{k_BT}{\pi a\langle\Delta r^2(t)\rangle\Gamma[1+\alpha(\omega)]_{t=1/\omega}}, \tag{3}$$

where

$$\alpha(\omega) = \left.\frac{\partial\ln\langle\Delta r^2(t)\rangle}{\partial\ln t}\right|_{t=1/\omega}. \tag{4}$$

From theses expressions, the single-point microrheological storage modulus $G_1'(\omega)$ and loss modulus $G_1''(\omega)$ are calculated,

$$G_1'(\omega) = |G^*(\omega)|\cos[\pi\alpha(\omega)/2],$$

$$G_1''(\omega) = |G^*(\omega)|\sin[\pi\alpha(\omega)/2]. \tag{5}$$

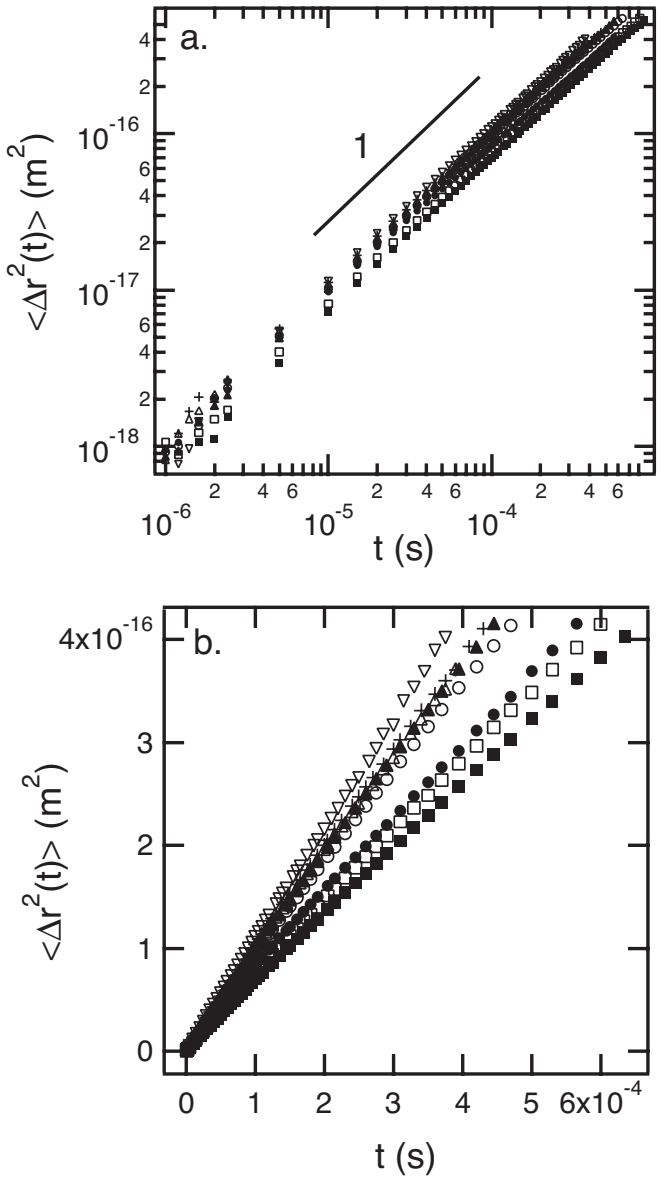

FIG. 2. (a) Mean-squared displacements of particles in 0.63 mg/ml F-actin with various average filament lengths, L, controlled by the addition of gelsolin. Filled square: unshortened F-actin ($L \approx 20$ μm); open square: $L \approx 5$ μm; filled circle: $L \approx 3$ μm; open circle: $L \approx 1.5$ μm; filled triangle: $L \approx 1.2$ μm; open up triangle: $L \approx 0.5$ μm; cross: $L \approx 0.15$ μm; and open down triangle: $L \approx 0.053$ μm). The solid line has a slope 1 for comparison. (b) Linear plots demonstrate the decrease in mean-squared displacement as the filament length increases.

We find that the above expressions are sufficient for calculating $G_1'(\omega)$ and $G_1''(\omega)$ for the majority of our experimental data. However, in regimes where $G_1'(\omega)$ and $G_1''(\omega)$ are expected to exhibit greater curvature, we apply a correction that includes the second-order logarithmic time derivatives, as described by Dasgupta *et al.* [37].

In the remainder of this paper, we investigate the dynamics of particles further by comparing our results to recent theoretical and experimental work, first the dilute, and then the entangled regimes. Before proceeding, we first note that

TABLE I. Gelsolin concentration, molar ratio of gelsoin to actin, calculated actin filament length, and scaling exponent of the mean-squared displacements shown in Fig. 2(a).

c_G (μg/ml)	$r_{G:A} \times 10^3$	L (μm)	α
62	51	0.053	1.01±0.004
21.9	18	0.15	0.99±0.004
6.6	5.4	0.5	0.99±0.004
2.8	2.3	1.2	1.00±0.003
2.2	1.8	1.5	0.99±0.005
1.1	0.9	3	0.95±0.004
0.6	0.5	5	0.97±0.003
0	0	20 (unshortened)	0.97±0.004

there are no significant differences in $\langle \Delta r^2(t) \rangle$ for particles preadsorbed with BSA versus those covalently grafted with PEG. Figure 5 shows the comparison of the mean-squared displacement for the PEG-coated particles with those of BSA-coated and plain PS particles. These results are consistent with recent multiple particle tracking results presented by Valentine *et al.* [38]. Second, our DWS results are in excellent agreement with previous reports of particle dynamics in entangled F-actin solutions. In Figure 6, we compare the mean-squared displacement with those measured by McGrath *et al.* using laser tracking [33] and the multiple particle tracking microrheology experiments of Liu *et al.* [45], correcting for small differences in particle size and actin concentrations between the measurements [46]. We also include the results of Ref. [30]. For similar noninteracting particle surface chemistries, the DWS experiments are found to extend the previously reported data to short time scales,

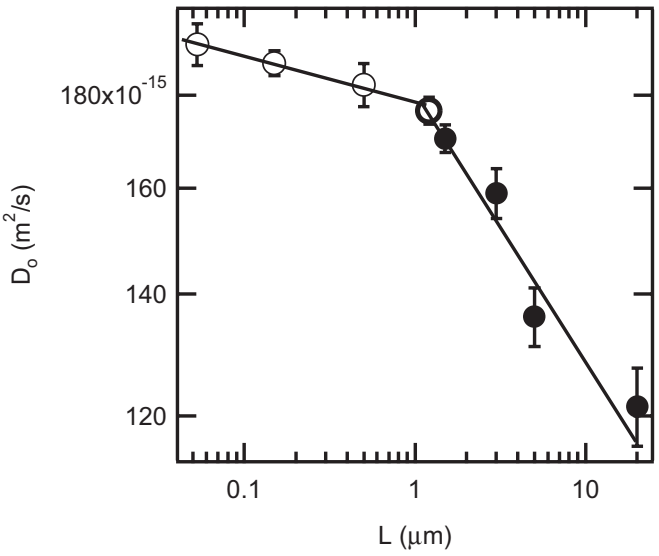

FIG. 3. The particle short-time diffusion coefficients as a function of actin filament length. The actin concentration is 0.63 mg/ml. The bold open circle corresponds to the point closest to the expected transition to the tightly entangled fluid regime. Lines are shown to guide the eye.

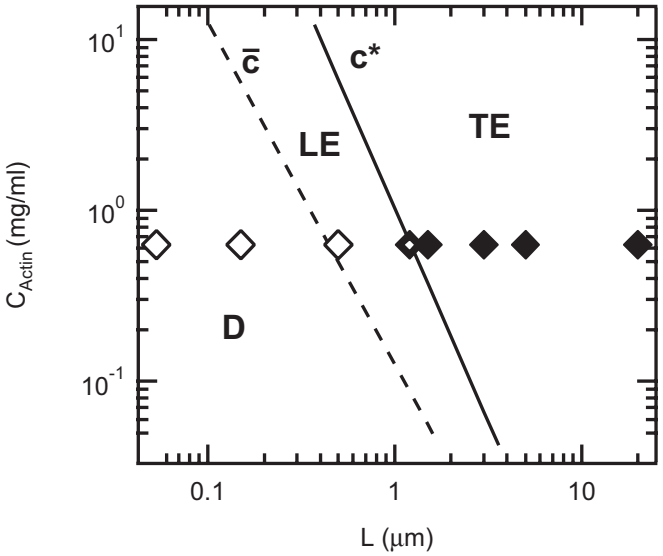

FIG. 4. The overlap concentration $\bar{c}$ and entanglement concentration c^* marking the boundaries between the dilute (D), loosely entangled (LE), and tightly entangled (TE) regimes are plotted as a function of filament length. The transition point of the initial diffusivity with filament length (Fig. 3) is in excellent agreement with the calculated transition to the tightly entangled regime, as shown by the bold open symbol.

with excellent quantitative agreement in the regions of overlapping lag times. This holds for the results of Ref. [33], as well as Ref. [45]. For comparison, we also plot the response of *untreated* polystyrene probe particles, a surface chemistry

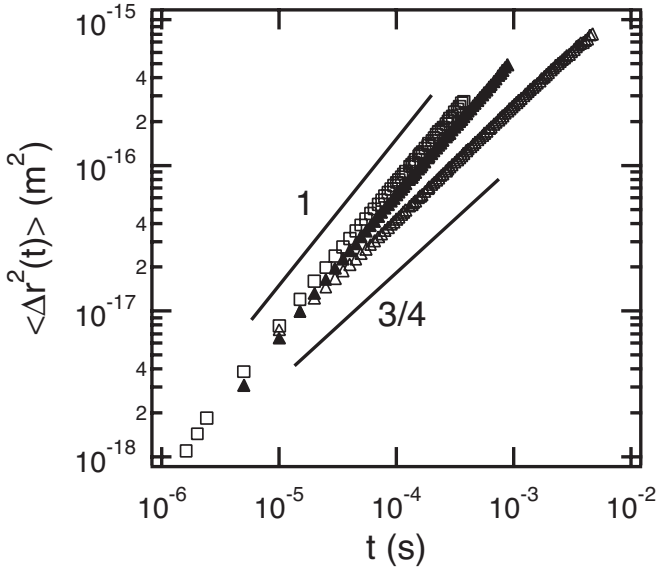

FIG. 5. Mean-squared displacements of particles in 0.63 mg/ml F-actin comparing three particle surface chemistries: untreated PS (open triangle); PS with adsorbed BSA (open square); PS with covalently attached PEG (filled triangle). The subdiffusive response of untreated PS particles, $\langle \Delta r^2(t) \rangle \sim t^{0.75}$, is in good agreement with previous microrheology studies. Both PEG and BSA-treated particles exhibit nearly identical responses with significantly less subdiffusion.

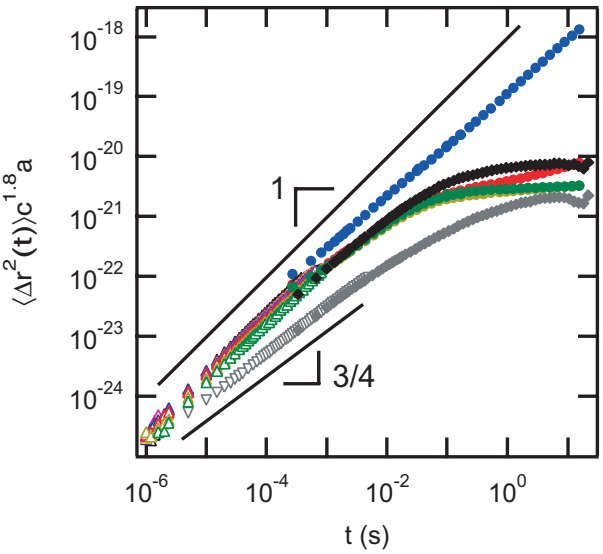

FIG. 6. (Color online) DWS data using $2a=1.053$ μm particles (open down triangle, black: PS with adsorbed BSA; gray: untreated PS) [30] and $2a=1.072$ μm (open up triangle, green: unshortened F-actin ($L \approx 20$ μm); dark yellow: $L \approx 5$ μm; red: $L \approx 3$ μm; violet: $L \approx 1.5$ μm; orange: $L \approx 1.2$ μm; blue: $L \approx 0.5$ μm; pink: $L \approx 0.15$ μm; black: $L \approx 0.053$ μm) in 0.63 mg/ml F-actin is in good agreement with measurements using laser tracking microrheology for $2a=0.914$ μm (filled diamond, black: PS adsorbed with BSA; gray: untreated PS) in 1.0 mg/ml unshortened F-actin [33] and multiple particle tracking for $2a=0.84$ μm PS coated with PEG (filled circle, green:$L \approx 17$ μm; dark yellow:$L \approx 5$ μm; red: $L \approx 2$ μm; blue: $L \approx 0.5$ μm) [45] in 1.0 mg/ml F-actin. Differences in the particle size and F-actin concentration are adjusted by the concentration dependence of the modulus and particle radius $c^{1.8}a$ [46]. $\langle \Delta r^2(t) \rangle$ and a have units of length in meters and c is in mg/ml. Two solid lines have slopes 1 and 3/4, respectively, for comparison.

known to interact strongly with filaments, taken from Refs. [30,33]. Note that these differ substantially, both in magnitude and scaling dependence on the lag time. In these earlier studies, it was shown that $\langle \Delta r^2(t) \rangle \sim t^{3/4}$, as expected for semiflexible filaments.

B. Dilute solutions

As discussed in Sec. III A, solutions of 0.63 mg/mL F-actin with average filament lengths less than approximately $L=1$ μm are below the expected entanglement transition. This enables us to use the generalized Stokes-Einstein equation to compare the measured particle dynamics with theory describing the dilute solution rheology of rodlike and semiflexible polymers [39,40].

In the classic theory of rodlike polymers, the molecules are commonly treated as smooth cylinders of length L and diameter d. Each rodlike polymer undergoes translational and rotational Brownian motion. In an oscillatory shearing flow for dilute suspensions of rods, where the polymers do not exert steric constraints on each other, the storage and loss moduli are [39]

$$G'(\omega) = \frac{3}{5} \nu k_B T \frac{\tau^2 \omega^2}{1 + \omega^2 \tau^2}, \tag{6}$$

$$G''(\omega) = \frac{3}{5}\nu k_B T\left(\frac{\tau^2\omega^2}{1+\omega^2\tau^2} + \frac{1}{3}\tau\omega\right) + \omega\eta_s, \tag{7}$$

where ν is the number of rods per unit volume, η_s is the viscosity of solvent, and τ is the rotational relaxation time $\tau=(6D_{r0})^{-1}$ with the rotational diffusion coefficient $D_{r0}=[3k_BT\ln(L/d)]/(\pi\eta_s L^3)$. Equations (6) and (7) should accurately describe the low-frequency microrheology of actin filaments, which are much smaller than the persistence length, and therefore more rodlike. However, as the filament length increases, the semiflexibility of the molecule will potentially contribute to the stress through intramolecular relaxation modes.

Shankar *et al.* find that the viscoelasticity of solutions of semiflexible rods at higher frequencies differs from that of rigid rods [40]. Briefly, the theoretical model considers the inextensible wormlike chain (WLC) as an effectively extensible rod with a frequency-dependent longitudinal modulus $B(\omega)$ due to the existence of transverse thermal fluctuations [12,19,40],

$$B(\omega) = \frac{\kappa^2}{k_B T}\left(\frac{2i\omega\zeta_\perp}{\kappa}\right)^{3/4}, \tag{8}$$

where κ is the filament bending modulus and $\zeta_\perp$ is the friction coefficient for transverse fluctuations, $\zeta_\perp=4\pi\eta_s/\ln(\xi_\perp/d)$ corresponding to a hydrodynamic screening length $\xi_\perp$ [12,40]. The polymer contribution to the stress is obtained by summing three separate terms,

$$\sigma_{polymer} = \sigma_{curv} + \sigma_{orient} + \sigma_{tens}, \tag{9}$$

where σ_{tens} is the stress arising from the inextensibility of the chain, σ_{curv} is the "curvature stress," which includes both purely mechanical bending forces and the orientational entropy of the chain links, and σ_{orient} is the residual contribution from the orientational entropy of the chain ends. Shankar *et al.* [40] derived analytical approximations of the complex modulus for each stress contribution in the form of the intrinsic modulus $[G^*(\omega)]=[G^*(\omega)-i\omega\eta_s]/\nu$,

$$[G^*_{tens}(\omega)] \cong \frac{1}{15}LB(\omega)\left[1 - \frac{\tanh[\lambda(\omega_1)/2]}{\lambda(\omega_1)/2}\right]\frac{\omega}{\omega_1}, \tag{10}$$

$$\left[G^*_{curv}(\omega)\right] \cong \frac{3}{2^{3/4}}\frac{L}{L_P}(i\omega_2\tau_\perp)^{-1/4}[G^*_{tens}(\omega)] + \frac{3k_BT}{2^{3/4}10}(i\omega_3\tau_\perp)^{1/4}\frac{\omega}{\omega_3}, \tag{11}$$

and

$$[G^*_{orient}(\omega)] = \frac{3}{5}k_BT\frac{i\omega\tau_{rod}}{1+i\omega\tau_{rod}}, \tag{12}$$

where $\lambda(\omega_1)=[i\omega_1\zeta_\Pi L^2/B(\omega_1)]^{1/2}$, $\omega_i=\omega-iC_j\alpha_o^4\tau_\perp^{-1}$, $\alpha_j=(2j+1)\pi/2$, $\tau_\perp=\zeta_\perp L^4/\kappa$, $\tau_\Pi=[\varsigma_\Pi/(2\zeta_\perp)]^3\times[\zeta_\Pi L^8/(k_BT\times L_P^5)]$, $\tau_{rod}=\zeta_\perp L^3/(72k_BT)$, and $\zeta_\Pi=2\pi\eta_s/\ln(\xi_\perp/d)$ corresponding to the friction coefficient for a motion of the chain parallel to its own contour length. The numerical constants C_j optimize the fit of this approximate solution to the exact theory, and are given as $C_1=0.14$, $C_2=0.72$, and $C_3=1.26$ [40].

A comparison between the experimental moduli in the dilute limit and the above theories is shown in Fig. 7. For the shortest filament length [$L=0.053$ μm, Fig. 7(a)], the storage and loss moduli are in qualitative and quantitative agreement with the calculated values from both theories. In this case, the filaments are short enough that the dominant contribution to the moduli comes from the rotational relaxation of the molecules, even at the high frequencies probed here by DWS. This is particularly apparent from the storage modulus, which scales with frequency as $G'(\omega)\sim\omega^2$. As indicated from $G'(\omega)$ in Fig. 7(a), the experiments exhibit a characteristic relaxation time scale intermediate to those calculated for the rigid rod theory ($\tau=5.2$ μs) and semiflexible theory ($\tau_{rod}=1.9$ μs). By fitting Eqs. (6) and (7) to our experimental data, we find the rotational relaxation time $\tau=2.65$ μs. The next largest filament length ($L=0.15$ μm) is in qualitative agreement with the transition in $G'(\omega)$ to the plateau value derived from both theories, as shown in Fig. 7(b). The quantitative deviations at the extremes of the experimental frequency range probably reflect the finite polydispersity of the filaments.

As the filament length increases, the frequency for rotational relaxation is significantly smaller than the frequencies probed by DWS. At high frequencies ($\omega\gg\tau_{rod}^{-1}$), the storage modulus plateaus in the rodlike theory, whereas intramolecular modes contribute to the moduli for polymers with finite flexibility. Figures 7(c) and 7(d) show that $G'(\omega)$ continues to increase with frequency for $L=0.5$ μm and $L=1.2$ μm, similar to the behavior expected from the theory of Shankar *et al.* [40]. Although the qualitative behavior for $G'(\omega)$ is similar, the experimental values appear to be shifted to lower frequencies relative to the theory. The magnitude of the shift, however, decreases as the filament length increases; experiments for $L=1.2$ μm [Fig. 7(d)] are much closer to the theoretical values. This may reflect the fact that Eqs. (10)–(12) apply rigorously for L/L_p between 1/8 and 1, a condition that longer filaments are closer to satisfying. We note that, in all cases, $G''(\omega)$ is significantly larger than $G'(\omega)$, and in good quantitative agreement with theory.

C. Tightly entangled solutions

For the solutions of filament lengths greater than $L=1.2$ μm, we expect the particle motion to be constrained by the surrounding entangled polymer network. The theory of entangled solutions of semiflexible polymers is formulated by Morse, and is developed based on the tube model with the entanglement length, L_e which is on the order of the distance between collisions of the polymer with the walls of the tube [19]. Since the experiments here measure particle dynamics on time scales significantly shorter than the entanglement relaxation time $\tau_e\sim\zeta_\perp L_e^4/(k_BTL_P)$, the complex modulus in this limit of corresponding frequencies is dominated by the tension contribution

$$G^*(\omega)|_{\omega\gg1/\tau_e} \approx G^*_{tension}(\omega) \sim \frac{2^{3/4}\rho k_BT}{15L_P}\left(i\omega\frac{\zeta_\perp L_P^3}{k_BT}\right)^{3/4}, \tag{13}$$

which leads to a frequency scaling for the moduli $G'(\omega)\sim G''(\omega)\sim\omega^{3/4}$. This scaling has been reported for probe mi-

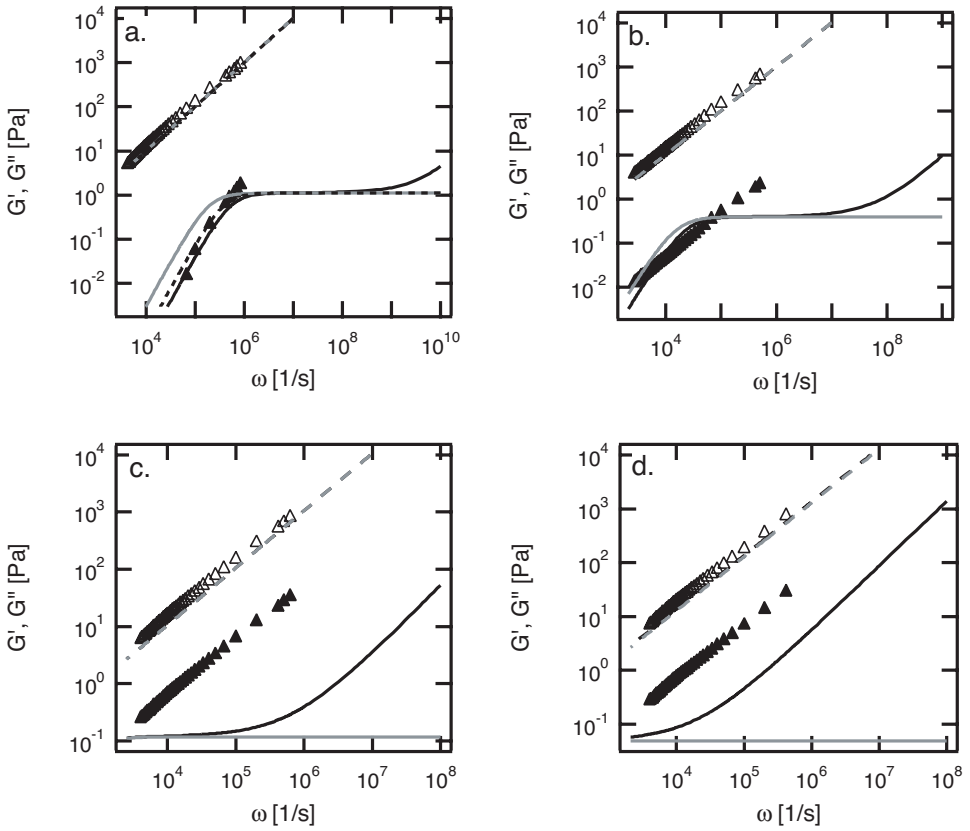

FIG. 7. The experimental $G'(\omega)$ (filled triangle) and $G''(\omega)$ (open triangle) calculated from the particle dynamics using the generalized Stokes-Einstein relationship compared to the dilute solution theories of rods [$G'(\omega)$, solid gray line; $G''(\omega)$, dashed gray line] and semiflexible [$G'(\omega)$, solid black line; $G''(\omega)$, dashed black line] polymer rheology calculated using Eqs. (10)–(12). The plots show four average filament lengths in the dilute regime: (a) $L \approx 0.053$ μm. The black dotted lines are the moduli calculated using Eqs. (6) and (7) with the fitted time scale $\tau = 2.65$ μs; (b) $L \approx 0.15$ μm; (c) $L \approx 0.5$ μm; and (d) $L \approx 1.2$ μm.

crorheology studies [25,28]. However, it is critical to note that previous experiments were performed using particle surface chemistries that promote filament adhesion to the particles, in contrast to the probe surface chemistries used in this study [33]. Indeed, when untreated PS particles are used, we recover a 3/4 scaling for the mean-squared displacement, as shown in Figs. 5 and 6. Under conditions where filament adhesion is minimized, we found previously that particle dynamics in entangled F-actin solutions are consistent with the formation of a depletion layer around the particles of thickness Δ, which scaled with the particle size [30].

Figures 8(a) and 8(b) show the storage and loss moduli calculated using the GSER for entangled solutions of various filament lengths. Both moduli increase as the filament length increases. This in itself is interesting, because the theory of entangled semiflexible polymer rheology does not predict a filament length dependence for the tension modulus; only the lower frequency orientation stress should exhibit this dependence. Furthermore, when compared with Eq. (11), there are both qualitative and quantitative differences between theory and our experiments. The experimental loss modulus has a systematically higher frequency scaling than the anticipated $G''(\omega) \sim \omega^{3/4}$. This behavior is again consistent with depletion of polymer near the particle surfaces [30]. The bulk modulus $G^*_{bulk}(\omega)$ and DWS-based single-point microrheology measurements $G^*_1(\omega)$ are used to determine Δ by the viscoelastic shell model of Levine and Lubensky [41],

$$G^*_1(\omega) = \frac{2G^*_{bulk}(\omega)[\chi'' - 2\beta^5\chi']}{4\beta^6\chi' - 9\beta^5\chi\chi' - 9\beta\chi'^2 - 15\beta\chi' + 2\chi\chi''}, \tag{14}$$

where $\beta = a/(a+\Delta)$, $\chi = -G^*_{bulk}(\omega)/(i\omega\eta_s)$, $\chi' = \chi - 1$, $\chi'' = 3 + 2\chi$, and η_s is the buffer viscosity. The shell model, illustrated in Fig. 9, essentially provides a hydrodynamic length scale that characterizes the perturbation of the polymer network structure surrounding the particles. As a coarse-grained approach, the continuous gradient of polymer segment density around the particle is replaced with a step change, assuming that the depleted corona is dominated by the viscous response of the solvent. We note that the shell model has also been successfully used to characterize the depletion layer thicknesses for particles dispersed in entangled DNA solutions [42].

The experimental results of Chae and Furst [30] for microspheres dispersed in solutions of entangled, unshortened F-actin filaments at 0.63 mg/ml, are summarized in Fig. 10(a). Similarly, shell thicknesses calculated from the current microrheolgy results for solutions of increasing filament length (Fig. 8) are shown in Fig. 10(b). In the previous case

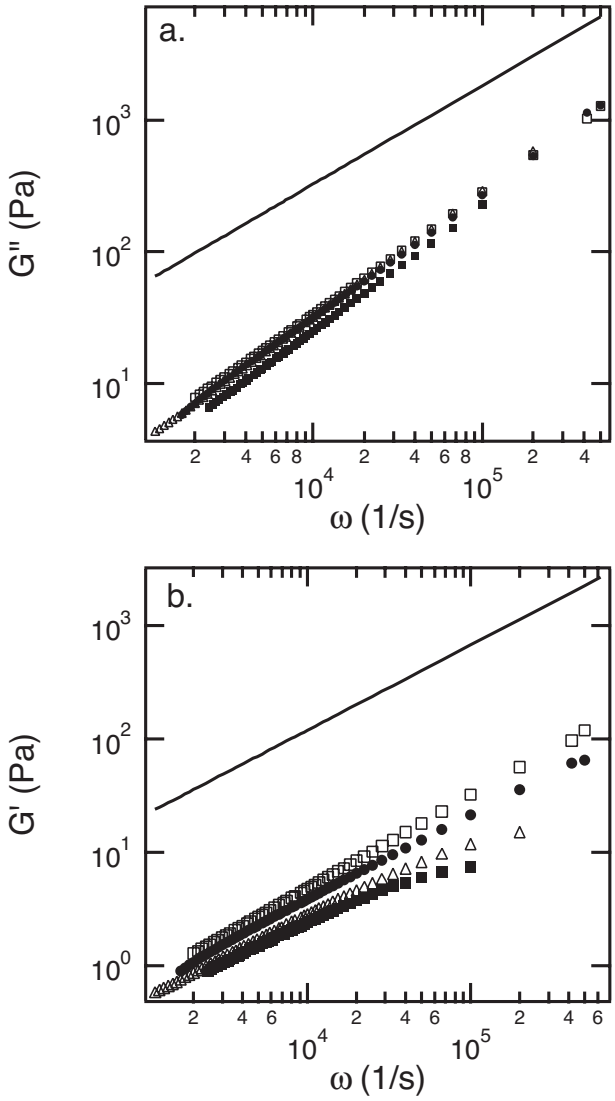

FIG. 8. (a) $G''(\omega)$ and (b) $G'(\omega)$ calculated using the generalized Stokes-Einstein relationship in the tightly entangled regime for four filament lengths (filled square: $L \approx 1.5$ μm; open triangle: $L \approx 3$ μm; filled circle: $L \approx 5$ μm; and open square: $L \approx 20$ μm) compared to the theory of entangled solution rheology of semiflexible polymers (solid lines) using Eq. (13) [12].

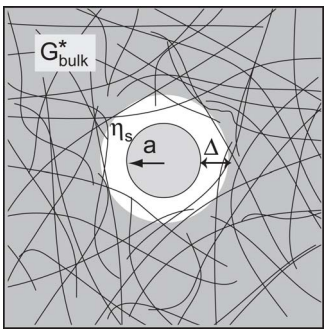

FIG. 9. Illustration of the viscoelastic shell model used to calculate the depletion layer thickness Δ.

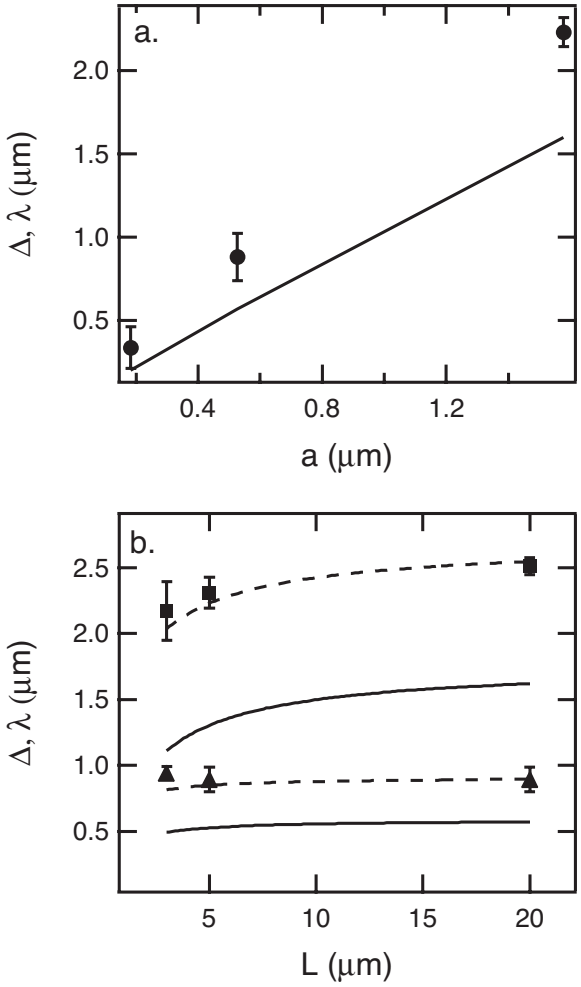

FIG. 10. The depletion shell thickness Δ (symbols) calculated using the viscoelastic shell model and nonlocality length, λ (lines) from PRISM theory as a function of particle size [(a) shell thickness data obtained from Ref. [30] and filament length for two particle sizes, (b) square: 3.21 μm diameter; and triangle: 1.07 μm diameter.] In (b), the upper and lower solid lines show the calculated nonlocality length for the larger and smaller particles, respectively. They have been shifted (dashed lines) to compare the trends.

[Fig. 10(a)], Δ increases as the particle radius increases. Note in Fig. 10(b) that this particle size dependence is reproduced when we examine two particle sizes in the solutions of varying filament length. More interestingly, Δ appears to be nearly insensitive to the filament lengths. For 1 μm particles, Δ is constant within the error of the measurements, while there is a slight increase in Δ with increasing filament length for 3 μm particles.

The existence of depletion layers around particles in entangled F-actin networks was first hypothesized by Morse, who noted that the excluded orientations of infinitely long, rigid filaments should result in a corona depleted of polymer segments with a thickness proportional to the particle radius [19]. The issue of depletion for all regimes of particle size and polymer length has recently been addressed from first principles for particles in model rodlike suspensions using the modified PRISM theory [9]. The theory accounts for nonlocal entropic repulsions and the loss of conformational en-

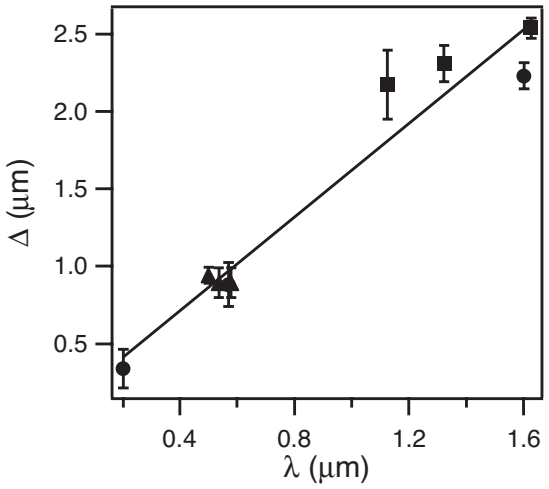

FIG. 11. The dependence of the depletion shell thickness Δ on both particle size and filament length is collapsed onto a single curve by the nonlocality length λ [circle: data from Fig. 10(a); square: 3.21 μm diameter particles shown in Fig. 10(b); triangle: 1.07 μm diameter shown in Fig. 10(b)]. Note that the depletion shell thickness is 1.5–1.9 times larger than λ. The line is a least-squares fit to the data.

tropy associated with polymer segments close to the impenetrable particles. In the theoretical formulation, a nonlocal disturbance, λ, quantifies the range that the particle perturbs the polymer conformation. For particles with radii a much larger than the polymer radius of gyration R_g ($a/R_g \gg 1$), the classical result $\lambda \sim R_g$ is anticipated for dilute colloids, while for $a/R_g \ll 1$, $\lambda \sim a$, similar to Morse's conjecture. The theoretical results yield an empirical expression for λ in the form of an interpolation function between the $a/R_g \gg 1$ and $a/R_g \ll 1$ limits. For ideal (noninteracting) rods,

$$\lambda^{-1} = L^{-1} + [(1-\phi^2)1.12a]^{-1}, \tag{15}$$

which is reported to satisfy thermodynamic consistency to within 15% [9].

Values of λ are calculated for the corresponding filament length and particle diameters used in our studies. Figure 11 shows the remarkable similarity of λ and Δ, demonstrating that the empirical nonlocality length for sphere-rod mixtures from PRISM theory [Eq. (15)] qualitatively captures the dependence of Δ on both particle size and filament length. Similar to Δ, λ increases with particle radius for $L \gg a$, as shown in Fig. 10(a). Likewise, Fig. 10(b) shows λ increases slightly for larger spheres as the filament length increases, but is nearly constant for the smaller particle diameters. In Fig. 11, we plot Δ versus λ, which demonstrates that Eq. (15) collapses all of the data, regardless of filament length and particle diameter. Interestingly, for all cases, λ is systematically lower than Δ by a factor of 1.5 to 1.9. This observation is similar to those reported for depletion layers in entangled DNA solutions, where it was found that Δ was a factor of approximately 1.5 larger than the expected shell thickness [42]. It was suggested that the discrepancy could be accounted for by the penetration of the solvent into the periphery of the shell, which is not captured by Eq. (12).

IV. CONCLUSIONS

The dynamics of colloidal particles dispersed in semiflexible polymer solutions of F-actin with different average filament lengths were investigated under conditions where the attractive interactions between filaments and particles are reduced. Two distinct regimes of the particle dynamics were found as a function of filament length, in good agreement with the expected transition from the dilute to the tightly entangled regime. Particle dynamics were then compared to theories of dilute and entangled rodlike and semiflexible polymers using the generalized Stokes-Einstein equation. In the dilute regime, the particle dynamics were in good agreement with the theoretical models of rodlike and semiflexible polymer solutions. However, in the entangled regime, the particle dynamics reflect the formation of a local depletion layer. Using the viscoselastic shell model, we found that the depletion layer thickness is consistent with the empirical nonlocality length obtained from PRISM theory. Importantly, the nonlocality length describes both the filament length and particle size dependence of the depletion layer thickness in entangled F-actin solutions.

As these experiments have shown, microrheology is well suited to quantify the structure and response of highly local effects, such as depletion. A significant advantage of high-frequency methods DWS is the relatively small amount of structural rearrangement the polymer network is expected to undergo on the time scale of the particle motion. In this way, microrheology effectively becomes a "hydrodynamic scattering" experiment that probes local polymer structure over a region which scales as the particle size. A disadvantage, however, is that the corresponding high-frequency bulk rheology, which is used to compare with single-point measurements, may not be known *a priori*. New approaches employing high-frequency laser tracking microrheology [43,44], which can measure two-particle correlations in addition to the single-particle microrheological response, offer a potential solution for this emerging application. As a final caveat, the ability to probe local polymer structure surrounding embedded particles is limited at high frequencies by the viscous penetration depth $\delta^* \sim \sqrt{2G^*/\rho\omega^2}$ [24]. While the penetration length in the studies reported here are on the order of ten times the particle radius, inertial effects will certainly become important at higher frequencies and larger particle sizes.

ACKNOWLEDGMENTS

We thank Jiayu Liu, David Weitz, James McGrath, and Scot Kuo for providing their original microrheology data. This research was supported by the ACS Petroleum Research Fund (Grant No. 41237-G7), NSF (Grant No. DBI-0304051), and the DuPont Young Investigator Program.

[1] M. Fuchs and K. S. Schweizer, J. Phys.: Condens. Matter **14**, R239 (2002).
[2] W. C. K. Poon, J. Phys.: Condens. Matter **14**, R859 (2002).
[3] R. G. Larson, *The Structure and Rheology of Complex Fluids* (Oxford University Press, New York, 1999).
[4] Y. L. Chen and K. S. Schweizer, Langmuir **18**, 7354 (2002).
[5] S. Asakura and F. Oosawa, J. Chem. Phys. **22**, 1255 (1954).
[6] A. Gast, C. Hall, and W. Russel, J. Colloid Interface Sci. **95**, 251 (1983).
[7] S. M. Ilett, A. Orrock, W. C. K. Poon, and P. N. Pusey, Phys. Rev. E **51**, 1344 (1995).
[8] D. G. A. L. Aarts, R. Tuinier, and H. N. W. Lekkerkerker, J. Phys.: Condens. Matter **14**, 7551 (2002).
[9] Y. L. Chen and K. S. Schweizer, J. Phys. Chem. B **108**, 6687 (2004).
[10] A. Tuteja, M. E. Mackay, C. J. Hawker, and B. V. Horn, Macromolecules **38**, 8000 (2005).
[11] A. Kulkarni and C. Zukoski, J. Cryst. Growth **232**, 156 (2001).
[12] D. C. Morse, Macromolecules **31**, 7030 (1998).
[13] C. F. Schmidt, M. Bärmann, G. Isenberg, and E. Sackmann, Macromolecules **22**, 3638 (1989).
[14] K. M. Addas, C. F. Schmidt, and J. X. Tang, Phys. Rev. E **70**, 021503 (2004).
[15] Gijsberta H. Koenderink, Stefano Sacanna, Dirk G. A. L. Aarts, and A. P. Philipse, Phys. Rev. E **69**, 021804 (2004).
[16] S. Biggs, D. C. Prieve, and R. R. Dagastine, Langmuir **21**, 5421–5428 (2005).
[17] L. Helden, R. Roth, G. H. Koenderink, P. Leiderer, and C. Bechinger, Phys. Rev. Lett. **90**, 048301 (2003).
[18] M. Piech and J. Y. Walz, Langmuir **16**, 7895 (2000).
[19] D. C. Morse, Macromolecules **31**, 7044 (1998).
[20] A. Ott, M. Magnasco, A. Simon, and A. Libchaber, Phys. Rev. E **48**, R1642 (1993).
[21] H. Isambert, P. Venier, A. Maggs, A. Fattoum, R. Kassab, D. Pantoloni, and M. Carlier, J. Biol. Chem. **270**, 11437 (1995).
[22] D. Bray, *Cell Movement* (Garland, New York, 2001).
[23] L. Le Goff, O. Hallatschek, E. Frey, and F. Amblard, Phys. Rev. Lett. **89**, 258101 (2002).
[24] F. Gittes, B. Schnurr, P. D. Olmsted, F. C. MacKintosh, and C. F. Schmidt, Phys. Rev. Lett. **79**, 3286 (1997).
[25] T. Gisler and D. A. Weitz, Phys. Rev. Lett. **82**, 1606 (1999).
[26] F. C. MacKintosh and P. Janmey, Curr. Opin. Solid State Mater. Sci. **2**, 350 (1997).
[27] J. Käs, H. Strey, and E. Sackmann, Nature **368**, 226 (1994).
[28] A. Palmer, T. G. Mason, J. Xu, S. C. Kuo, and D. Wirtz, Biophys. J. **76**, 1063 (1999).
[29] S. J. Kron and T. A. Spudich, Proc. Natl. Acad. Sci. U.S.A. **83**, 6272 (1986).
[30] B. S. Chae and E. M. Furst, Langmuir **21**, 3084 (2005).
[31] C. F. Schmidt, M. Bärmann, G. Isenberg, and E. Sackmann, Macromolecules **22**, 3638 (1989).
[32] P. A. Janmey, J. Peetermans, K. S. Zaner, T. P. Stossel, and T. Tanaka, J. Biol. Chem. **261**, 8357 (1986).
[33] J. L. McGrath, J. H. Hartwig, and S. C. Kuo, Biophys. J. **79**, 3258 (2000).
[34] D. J. Pine, D. A. Weitz, J. X. Zhu, and E. Herbolzheimer, J. Phys. (France) **51**, 2101 (1990).
[35] B. Hinner, M. Tempel, E. Sackmann, K. Kroy, and E. Frey, Phys. Rev. Lett. **81**, 2614 (1998).
[36] T. G. Mason, Rheol. Acta **39**, 371 (2000).
[37] B. R. Dasgupta, S. Y. Tee, J. C. Crocker, B. J. Frisken, and D. A. Weitz, Phys. Rev. E **65**, 051505 (2002).
[38] M. T. Valentine, Z. E. Perlman, M. L. Gardel, J. H. Shin, P. Matsudaira, T. J. Mitchison, and D. A. Weitz, Biophys. J. **86**, 4004 (2004).
[39] M. Doi and S. F. Edwards, *The Theory of Polymer Dynamics* (Oxford University Press, New York, 1986).
[40] V. Shankar, M. Pasquali, and D. C. Morse, J. Rheol. **46**, 1111 (2002).
[41] A. J. Levine and T. C. Lubensky, Phys. Rev. E **63**, 041510 (2001).
[42] D. T. Chen, E. R. Weeks, J. C. Crocker, M. F. Islam, R. Verma, J. Gruber, A. J. Levine, T. C. Lubensky, and A. G. Yodh, Phys. Rev. Lett. **90**, 108301 (2003).
[43] L. Starrs and P. Bartlett, Faraday Discuss. **123**, 323 (2003).
[44] M. Buchanan, M. Atakhorrami, J. F. Palierne, F. C. MacKintosh, and C. F. Schmidt, Phys. Rev. E **72**, 011504 (2005).
[45] J. Liu, M. L. Gardel, K. Kroy, E. Frey, B. D. Hoffman, J. C. Crocker, A. R. Bausch, and D. A. Weitz, Phys. Rev. Lett. **96**, 118104 (2006).
[46] M. L. Gardel, M. T. Valentine, J. C. Crocker, A. R. Bausch, and D. A. Weitz, Phys. Rev. Lett. **91**, 158302 (2003).